JOURNAL OF SPACECRAFT AND ROCKETS
Vol. 36, No. 6, November–December 1999

Nonlinear Behavior of Space Shuttle Superlightweight Tank Under End-of-Flight Loads

Michael P. Nemeth,* Richard D. Young,† Timothy J. Collins,‡ and James H. Starnes Jr.§
NASA Langley Research Center, Hampton, Virginia 23681-2199

Results of elastic, linear-bifurcation buckling and nonlinear analyses of the new Space Shuttle superlightweight external liquid-oxygen tank are presented for an important end-of-flight loading condition. These results illustrate an important type of response mode for thin-walled shells subjected to combined mechanical and thermal loads that may be encountered in the design of other liquid-fuel launch vehicles. Linear-bifurcation buckling analyses are presented that predict several nearly equal eigenvalues that correspond to local buckling modes in the aft dome of the liquid-oxygen tank. In contrast, the nonlinear response phenomenon is shown to consist of a short-wavelength bending deformation in the aft elliptical dome of the liquid-oxygen tank that grows in amplitude in a stable manner with increasing load. Imperfection sensitivity analyses are presented that show that the presence of several nearly equal eigenvalues does not lead to a premature general instability mode for the aft dome. For the linear-bifurcation and nonlinear analyses, the results show that accurate predictions of the response of the shell generally require a large-scale, high-fidelity, finite element model, and that a design based on a linear-bifurcation buckling analysis and a buckling-load knockdown factor is overly conservative. Results are also presented that show that the superlightweight liquid-oxygen tank can support loads in excess of approximately 1.9 times the values of the operational loads considered.

Introduction

THE International Space Station (ISS) is currently planned to occupy a 51.6-deg orbit. Construction of the ISS will require the Space Shuttle to deliver a large number of payloads to this high-inclination orbit. Until recently, achieving this orbit required the payload capacity of the orbiter be reduced by approximately 10,000 lb. To recover most of this lost payload capacity, and to minimize the number of Space Shuttle flights needed to build the ISS, NASA developed a new, lighter-weight external fuel tank for the Space Shuttle. This new design, referred to as the superlightweight (SLWT) external tank, is made primarily of an aluminum–lithium alloy and weighs approximately 58,000 lb, which is approximately 8000 lb lighter than the lightweight aluminum external tank previously in service. This 8000-lb weight savings translates into an 8000-lb increase in the payload capacity for the orbiter. The new SLWT tank flew for the first time on 2 June 1998 (Space Transportation System-mission 91).

As discussed in Ref. 1, an important consideration in the design of the SLWT tank is the nonlinear behavior of its thin-walled regions that experience compressive or shear stresses, and the sensitivity of this behavior to initial geometric imperfections. One component of the SLWT tank that experiences significant compressive stresses is the liquid-oxygen (LO_2) tank (see Fig. 1). Prior to launch, the weights of the liquid-hydrogen (LH_2) tank, the LO_2 tank, and the fuel are reacted at the solid-rocket-booster (SRB) attachment points, which causes meridional compressive stresses and shear stresses that extend into the nose of the SLWT tank. The nonlinear behavior of the SLWT LO_2 tank for two critical prelaunch loading conditions has been documented extensively in Refs. 1 and 2. The tank also experiences similar compressive and shear stresses during ascent, before the two solid rocket boosters (SRBs) are jettisoned. After the SRBs are jettisoned, and prior to orbital insertion, the LO_2 tank experiences compressive stresses in the aft end of the tank instead of the nose region.

The present paper presents results of elastic linear-bifurcation buckling and nonlinear analyses of the SLWT LO_2 tank that were conducted at the NASA Langley Research Center. The results are for a critical flight loading condition that occurs 423 s into the flight, after the SRBs are jettisoned and prior to orbital insertion (referred to herein as the 3g, end-of-flight loading condition). Two primary objectives of the present paper are to articulate the nonlinear response phenomena for this loading condition and to assess the relevance of the linear-bifurcation buckling analyses. Insight into the relevance of the linear-bifurcation buckling analyses for the present vehicle could be useful in the design of future liquid-fuel launch vehicles. These objectives are accomplished by using the large-scale finite element analysis approach of Refs. 1 and 2 to determine how much additional load, beyond the operational load level, the LO_2 tank can withstand before buckling or exhibiting undesirable wrinkle-like bending deformations that can lead to failure of the thermal protection system (TPS). Results have been presented in Refs. 1 and 2 for two full-scale structural tests that suggest that the finite element modeling approach is adequate for representing the nonlinear behavior of the SLWT LO_2 tank for the two prelaunch loadings considered. No structural test data were available for the 3g, end-of-flight loading condition. As part of this analysis approach, results are presented that can be used to gain insight into the performance of the TPS. The results illustrate a means that can be used to assess TPS performance of other, future liquid-fuel launch vehicles.

To accomplish the objectives of the present paper, a very brief overview of the SLWT LO_2 tank and intertank structure and the details of the loading condition are presented first. Then, details of the analysis code and finite element modeling are discussed very briefly and the load simulation is described. Next, results of elastic linear-bifurcation buckling analyses are presented, and then results of elastic nonlinear analyses for geometrically perfect and imperfect shells are presented. Details of the mesh convergence studies are also given. The imperfection sensitivity results include a discussion of the effects of modal interactions associated with several nearly equal linear-bifurcation buckling analysis eigenvalues. In the presentation, aspects of the finite element model, analyses, and results that may be relevant to the design of future liquid-fuel launch vehicles are discussed.

Received 27 April 1998; revision received 17 April 1999; accepted for publication 2 July 1999.

*Senior Research Engineer, Structural Mechanics Branch, Structures Division. Associate Fellow AIAA.
†Aerospace Engineer, Structural Mechanics Branch, Structures Division. Member AIAA.
‡Aerospace Engineer, Structural Mechanics Branch, Structures Division.
§Head, Structural Mechanics Branch, Structures Division. Fellow AIAA.

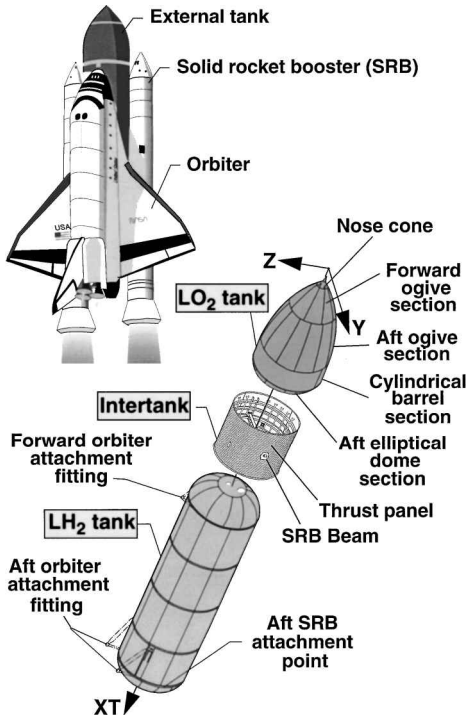

Fig. 1 Space Shuttle external tank components.

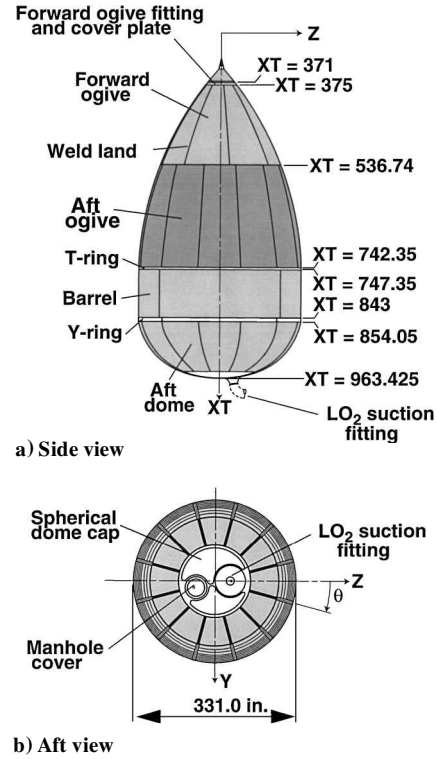

Fig. 2 Space Shuttle external LO_2 tank components; values of XT are given in inches.

Overview of the Structure

The Space Shuttle consists of the orbiter, two SRBs, and the external tank (ET), as shown in Fig. 1. The ET consists of a LO_2 tank, a LH_2 tank, and an intermediate structure called the intertank (Fig. 1). The intertank transmits the weight of the fuel, the ET structural weight, and the orbiter weight to the SRBs prior to launch and transmits thrust loads from the SRBs and the orbiter to the ET during ascent. The SLWT LO_2 tank is a thin-walled monocoque shell that is made primarily of 2195 aluminum–lithium alloy. The LO_2 tank is approximately 49 ft long and has a maximum diameter of approximately 27.5 ft, as indicated in Fig. 2. The LO_2 tank consists of a forward-ogive section made from 8 gore panels, an aft-ogive section made from 12 gore panels, a cylindrical barrel section made from 4 barrel panels, and an aft elliptical dome section made from 12 gore panels. The coordinate systems used to locate the elements of the LO_2 tank and the intertank are also shown in Fig. 2. The coordinates (XT, Y, Z) are typically referred to as the global coordinate system of the ET, and axial positions along the tank are indicated by the coordinate value of XT in units of inches. For example, the location of the junction between the forward and aft ogives is indicated by writing $XT = 536.74$ in. Cylindrical coordinates are also used and are given by (XT, r, θ), where a positive value of θ is measured from the positive Z axis toward the positive Y axis, as shown in Fig. 2b.

The LO_2 tank also has a forward ring frame with a T-shaped cross section that is referred to herein as the T-ring frame, and an aft ring frame with a Y-shaped cross section that is referred to herein as the Y-ring frame. These two ring frames support a baffle assembly that prevents the fuel from sloshing during ascent. The slosh baffle, a lightweight (approximately 455 lb), thin-walled structure, is supported by deep, thin-walled rings at each end that attach to the forward T-ring and the aft Y-ring frames. Other parts of the LO_2 tank include a nonstructural nose cone, a forged forward-ogive fitting and cover plate, an aft spherical dome cap that contains the LO_2 suction fitting and a covered manhole, and a vortex baffle attached to the base of the aft dome cap. The LO_2 tank gore and barrel panels are stretch formed, chemically milled, and then welded together. The panels are fabricated with substantial thickness tailoring to reduce structural weight. The panels are somewhat thicker at the welds to form a stiffenerlike region that is used as a weld land.

The intertank is a right-circular cylinder that is made from 2090 aluminum–lithium and 7075 aluminum alloys and is shown in Fig. 1. The approximately 22.5-ft-long intertank has a diameter of approximately 27.5 ft and consists of six 45-deg curved panels that are stiffened longitudinally with external hat stiffeners and are referred to herein as skin-stringer panels. The intertank also has two massive 45-deg curved panels, referred to as thrust panels (see Fig. 1), that are located perpendicular to the Y axis of the intertank and stiffened longitudinally with integrally machined external blade stiffeners. These eight panels are assembled into the intertank with mechanical fasteners and are attached to five large internal ring frames, a forward flange, and an aft flange. Longitudinal straps (referred to herein as roll ties) suppress lateral-torsional deflection of the ring frames. The main central ring frame, two thrust panel longerons, and the thrust panels are connected to each end of a tapered beam that is referred to herein as the SRB beam (see Fig. 1). The SRB beam spans the diameter of the intertank along the Y axis and has a maximum depth (in the XT direction) of approximately 43 in. at its midspan. Forged fittings (referred to herein as SRB thrust fittings) that are incapable of transmitting moments are fastened to the ends of the SRB beam. The primary role of the thrust panels is to diffuse the large axial loads introduced by the SRBs into the intertank and then into the LO_2 tank shell wall. The SRB beam compensates for the eccentricity of the concentrated loads introduced by the SRBs. The SRB beam also supports loads that are normal to the intertank (parallel to the SRB beam) at the SRB attachment points. The intertank also has a 46-in.-high by 52-in.-wide frame-reinforced nonstructural access door located along the cylinder generator at approximately $\theta = 146$ deg.

Critical Loading Condition

The $3g$, end-of-flight loading condition was identified and supplied by the members of the SLWT tank structural verification team at the NASA Marshall Space Flight Center and the Lockheed Martin Michoud Space Systems Division. This loading condition was identified as a critical loading condition that could cause buckling of the aft dome of the LO_2 tank and corresponds to a worst-case condition. As a result, no attempts are made in the present study to address issues of loading imperfections or perturbations. This loading condition corresponds to a partially filled LO_2 tank aft dome and an acceleration field given by $a_X = -3.040\,g$, $a_Y = 0.005\,g$, and $a_Z = -0.725\,g$, where g is the magnitude of the Earth's gravitational acceleration. The X subscript in the first acceleration corresponds to

the XT direction and is used in the present paper for convenience. Details of this loading condition are shown in Figs. 3–5. The loads consist of the inertial loads of the structural mass and the LO_2 mass, the ullage pressure exerted on the shell wall (Fig. 4), the LH_2 tank interface force and moment, and the thermal load associated with the cryogenic-fuel and aerodynamic heating. No SRB forces or aerodynamic pressure loads are present for this loading condition because the SRBs have been jettisoned by this point in the flight profile and the orbiter and external tank are essentially out of the dense part of the Earth's atmosphere. The inertial loads of the structural mass (magnitudes) are given by $m_s a_X = 72.38$ kips (1 kip = 1000 lb), $m_s a_Y = 0.12$ kips, and $m_s a_Z = 17.26$ kips. Similarly, the inertial loads of the LO_2 mass are given by $m_{LO_2} a_X = 588.67$ kips, $m_{LO_2} a_Y = 0.99$ kips, and $m_{LO_2} a_Z = 143.18$ kips (see Fig. 3). The interface force $\boldsymbol{F}$ and moment $\boldsymbol{M}$ between the intertank and the LH_2 tank are given by $\boldsymbol{F} = -661.050\boldsymbol{i} + 1.110\boldsymbol{j} - 160.440\boldsymbol{k}$ kips and $\boldsymbol{M} = -6.040\boldsymbol{i} - 51{,}428.720\boldsymbol{j} - 329.220\boldsymbol{k}$ in.-kips, where $\boldsymbol{i}$, $\boldsymbol{j}$, and $\boldsymbol{k}$ are standard orthonormal base vectors associated with the XT, Y, and Z axes, respectively.

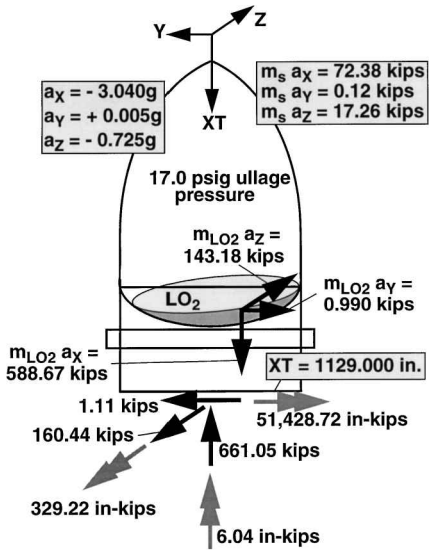

Fig. 3 Loads at 423 s into flight.

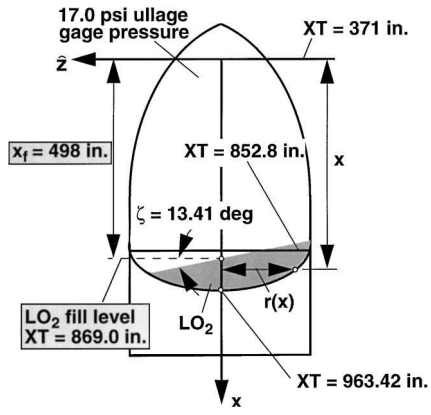

a) Side view

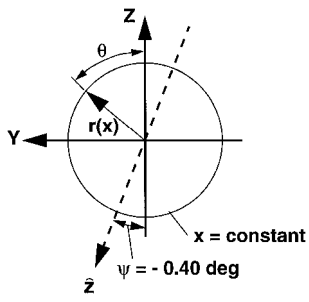

b) Top view

Fig. 4 LO_2 pressure distribution at 423 s into flight.

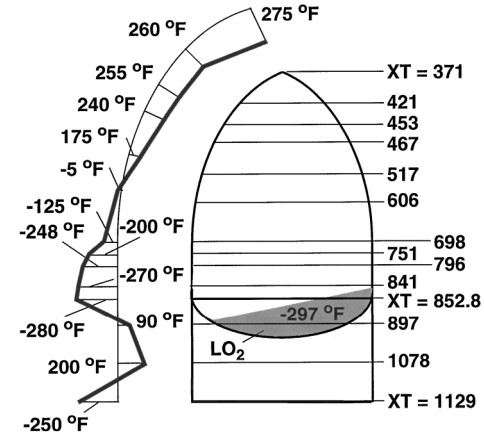

Fig. 5 Axisymmetric temperature profile at 423 s into flight; values of XT are given in inches.

As the Space Shuttle is accelerated, the LO_2 mass exerts pressure on the LO_2 tank shell wall. The resultant force of this pressure distribution corresponds to the inertial loads of the LO_2 that are given in Fig. 3. This pressure distribution is approximated by the situation depicted in Fig. 4 in which the LO_2 and its container are subjected to rigid-body motion and flow effects are neglected.

This approximate pressure distribution on the interior surface of the LO_2 tank is given by

$$p(x, \theta) = p_u \qquad \text{for} \qquad x \le x_s \tag{1}$$

$$p(x, \theta) = p_u - \gamma_{LO_2}(a_X/g)(x - x_s) \qquad \text{for} \qquad x > x_s \tag{2}$$

where x is a local axial coordinate that is measured from $XT = 371.00$ in., x_s is the local x coordinate of the surface of the fuel given by

$$x_s = x_f - r(x)[(a_Y/a_X)\sin\theta + (a_Z/a_X)\cos\theta] \tag{3}$$

where $x_f = 171.6$ in. is the local x coordinate of the fill level ($XT = 542.60$ in.) and $r(x)$ is the horizontal or polar radius of the tank. The ullage pressure is given by $p_u = 17.0$ psi gauge pressure and the specific weight of the LO_2 that was used in the present study is given by $\gamma_{LO_2} = 0.04123$ lb/in.^{3}. The local $\hat{z}$ axis shown in Fig. 4 corresponds to the axis of maximum inclination of the free surface of the LO_2 and is given by $\theta = 180$ deg $+ \psi$, where $\psi = \text{Tan}^{-1}(a_Y/a_Z) = -0.40$ deg. Similarly, the free surface of the LO_2 has an inclination angle in the x–$\hat{z}$ plane that is given by $\zeta = \text{Tan}^{-1}[\sqrt{(a_Y^2 + a_Z^2)}/|a_X|] = 13.41$ deg.

The temperature distribution that was used in the present study as an approximation associated with the cryogenic fuel and aerodynamic heating is shown in Fig. 5. The temperature distribution shown in Fig. 5 is axisymmetric and varies along the surface meridians in a piecewise-linear manner. The hottest place on the LO_2 tank and the intertank is the tip of the ogive (275°F), and the coldest is at the bottom region of the aft dome (−297°F). The nominal ambient temperature of the LO_2 tank and the intertank prior to fueling is 50°F. This temperature was used in the present study as the temperature at which thermal stresses in the LO_2 tank are absent.

Analysis Code and Finite Element Modeling

The results of the elastic, linear-bifurcation buckling and nonlinear analyses were obtained with the STAGS nonlinear structural analysis code for general shells.[3] STAGS was chosen for analyzing the SLWT tank because of its robust state-of-the-art nonlinear-equation solution algorithms and its general user-input capability that is convenient for modeling branched shells that are typically used for launch vehicles. The shell elements that were used to model the SLWT tank response are based on classical thin-shell theory. The use of these elements is justified because the ratio of the wall thickness to the minimum radius of curvature at each point of the undeformed LO_2 tank is generally much less than 0.1 and, as will

be shown, because the ratio of the largest thickness of the shell wall that forms a given deformation pattern to the smallest characteristic length of the deformation pattern is less than 0.1 (Ref. 2). A description of the attributes of STAGS and how the features of STAGS were used in the present study to model the SLWT LO_2 tank and intertank are presented in Refs. 3 and 4.

The finite element models of the SLWT tank that were used in the present study are very complex and include many structural details and the skin thickness variations or tailoring used to reduce structural weight; for example, see Ref. 4. Moreover, the details of the models are enormous and, as a result, are not presented herein; they are discussed in Refs. 1 and 4. Details of how the applied loads were simulated in the present study are presented subsequently.

Load Simulation

The basic approach used in the present study to simulate the actual $3g$, end-of-flight loading condition is to apply all accelerations and associated inertial and LO_2 pressure loads illustrated in Figs. 3 and 4 to the model. The thermal load was applied by introducing the axisymmetric temperature distribution shown in Fig. 5 as a temperature change from a nominal initial uniform temperature of 50°F. The bottom of the intertank, where the LH_2 tank interface force and moment act, was restrained so that the LH_2 tank interface force and moment become reactions, and rigid-body motion is eliminated. Next, the applied loads were separated into two groups. The first group contains the pressure that acts on the shell wall because of the acceleration of the LO_2 mass, the structural-mass inertial loads, and the inertial line loads that represent the acceleration of the slosh baffle mass that is located inside of the barrel section of the LO_2 tank. This group of loads was indentified by the SLWT tank structural verification team as the primary source of destabilizing compressive stresses in the LO_2 tank that may occur at load levels greater than the corresponding operational load level. The second group of loads consists of the thermal load and the LO_2 tank ullage pressure. The loads in the second group are constant in value, are part of the operational loads, and are considered to be passive loads when determining the stability margin of safety of the LO_2 tank. In performing linear-bifurcation buckling and nonlinear analyses with STAGS, two load factors, p_a and p_b, were assigned to the first (active) and second (passive) load groups, respectively. Values of $p_a = p_b = 1$ correspond to the loading condition that was mentioned earlier as the operational load level.

Results and Discussion

Three different finite element models were used in the present study to perform a limited convergence study in the analysis of the LO_2 tank subjected to the $3g$, end-of-flight loading condition. As a first step toward identifying an adequate model with as few degrees of freedom as necessary, elastic, linear-bifurcation buckling analyses were conducted. The passive loads associated with load factor p_b were applied to the STAGS models as a linear prebuckling stress state ($p_b = 1$) and the active (destabilizing) loads associated with load factor p_a were used to obtain the minimum eigenvalue. The models that were investigated had 76,900, 103,400, and 158,000 degrees of freedom. The model that was identified as adequate for predicting the linear-bifurcation buckling behavior is shown in Fig. 6 and corresponds to 158,000 degrees of freedom.

The first linear-bifurcation mode (referred to herein as the linear-bifurcation buckling mode) for the geometrically perfect shell is shown in Fig. 7 for the STAGS model with 158,000 degrees of freedom. The eigenvalue for this model corresponds to active loads that are approximately 1.526 times the magnitude of the corresponding operational loads shown in Figs. 3 and 4. This buckling mode is a localized, short-wavelength wrinkle in the forward part of the aft dome that extends from approximately $\theta = 98$ to 132 deg with its large-amplitude region centered approximately on $\theta = 112.5$ deg. The second through fourth linear-bifurcation modes are also localized, short-wavelength modes, similar to the mode shown in Fig. 7, with eigenvalues equal to 1.528, 1.540, and 1.541, respectively, which are all less than 1% higher than the lowest eigenvalue. The second linear-bifurcation mode, which is nearly identical to the first mode, is also in the forward part of the aft dome with its large-amplitude

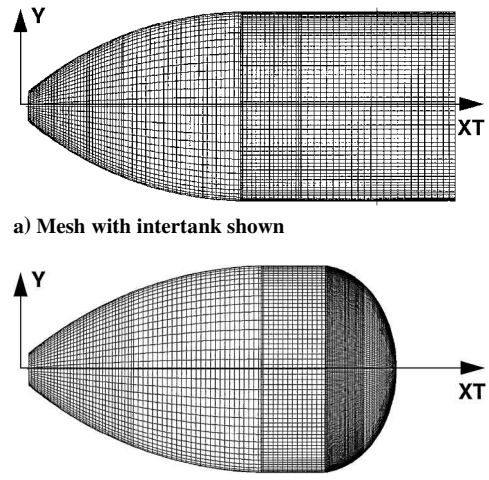

Fig. 6 Finite element mesh; 158,000 degrees of freedom.

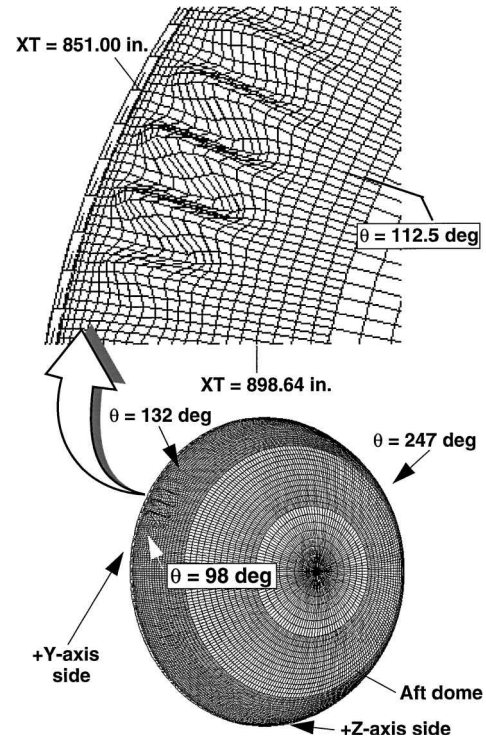

Fig. 7 Linear-bifurcation buckling mode; 158,000 degrees of freedom, p_a = 1.526 and p_b = 1.0.

region centered very close to $\theta = 112.5$ deg. The third and fourth modes are also nearly identical and located in the forward part of the aft dome, but their large-amplitude regions are centered approximately on $\theta = 247.5$ deg.

The nearly equal values of the first four eigenvalues, the short wavelength of the linear-bifurcation modes, and the large difference in location between the first two and last two linear-bifurcation modes led to the dense mesh refinement of the aft dome that is shown in Figs. 6 and 7. A uniform circumferential mesh refinement of the dome was used so as not to bias the location of the response and was facilitated by the use of the five-node and seven-node rectangular transition elements that are available in STAGS.[4] The 103,400- and 158,000-degree-of-freedom models have the same general mesh arrangement shown in Fig. 6, but the level of refinement of the forward part of the aft dome shown in Figs. 6 and 7 for the 158,000-degree-of-freedom model is essentially twice that of the 103,400-degree-of-freedom model. The lowest eigenvalues for the 103,400- and 158,000-degree-of-freedom models are given by $p_a = 1.536$ and 1.526, respectively. The smoothness of the buckling mode shown

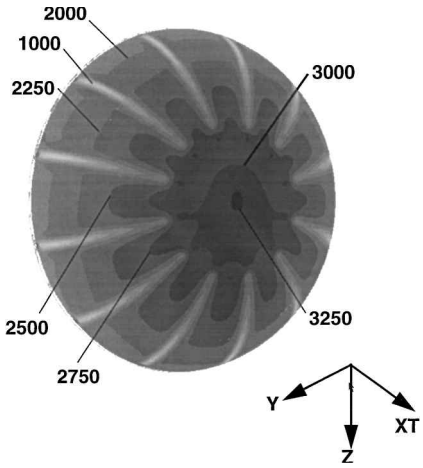

a) $p_a = p_b = 1.0$

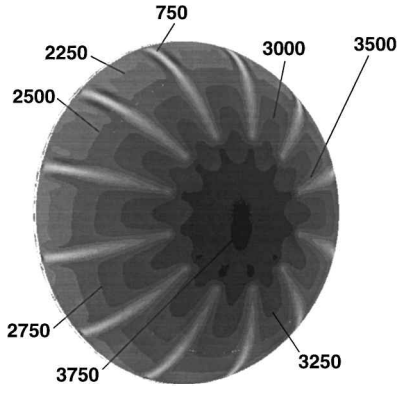

b) $p_a = 1.5$ and $p_b = 1.0$

Fig. 8 Meridional stress resultants in aft dome (pounds per inch).

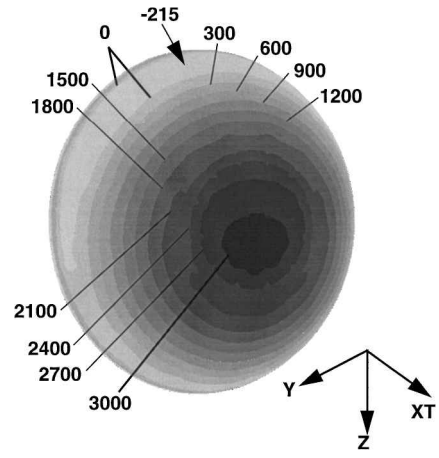

a) $p_a = p_b = 1.0$

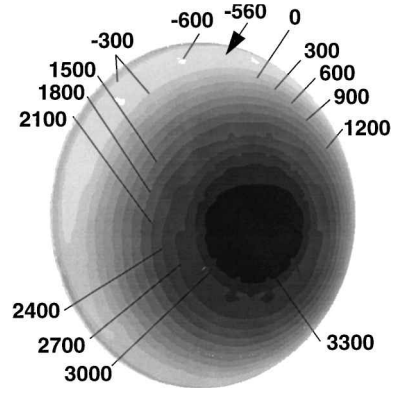

b) $p_a = 1.5$ and $p_b = 1.0$

Fig. 9 Circumferential stress resultants in aft dome (pounds per inch).

in Fig. 7 and the 1% difference in the eigenvalues suggest that the 158,000-degree-of-freedom model is adequate for representing the linear-bifurcation behavior of the LO_2 tank for this loading condition. In addition, the ratio of the largest thickness in the area of the buckling mode shown in Fig. 7 to its smallest characteristic length is less than 0.1, which suggests that finite elements that are based on classical thin-shell theory are adequate.

The 103,400- and 158,000-degree-of-freedom models were also used to obtain nonlinear solutions for geometrically perfect and imperfect shells. These solutions, which are in good agreement (within 5% of one another), indicate that the 158,000-degree-of-freedom model represents adequately the nonlinear behavior of the LO_2 tank for this loading condition. Thus, all subsequent results presented in this section were obtained with the 158,000-degree-of-freedom model.

The meridional stress resultant distribution (given in pounds per inch) in the aft dome, which was obtained from nonlinear analyses, is tensile and is shown in Fig. 8 for values of $p_a = p_b = 1$ and for $p_a = 1.5$ and $p_b = 1$. The lighter meridional bands of shading shown in Fig. 8 correspond to lower values of the meridional stress resultants along the weld lands. The meridional tension shown in Fig. 8 resists primarily the axial acceleration of the LO_2 mass and is responsible for the shortness of the wavelength of the linear-bifurcation buckling mode. The circumferential stress resultants in the aft dome that generate the linear bifurcation buckling modes are shown in Fig. 9 for values of $p_a = p_b = 1$ and for $p_a = 1.5$ and $p_b = 1$. These results show a region of circumferential compression ($90 \leq \theta \leq 270$ deg) that is also in the forward part of the aft dome, with the highest values of compression approximately near $\theta = 180$ deg. The average shell wall thickness in and around this region is 0.090 in.

An important concern that arose during the present study is the possiblity of high sensitivity to initial geometric imperfections that may be caused by the presence of four closely spaced eigenvalues of the linear-bifurcation buckling modes and that could lead to a premature collapse mode for the aft dome. This concern led to the use of an imperfection shape that is in the form of a linear combination of the first four linear-bifurcation buckling modes, described earlier in the present paper, in the nonlinear analyses of the imperfect shell. With this four-mode imperfection each mode possesses an equal degree of participation. Mathematically, this set of modes can be viewed loosely as a basis for an isotropic imperfection space, similar to a basis of a vector space. The first four modes were selected because they represent deformation states that the geometrically perfect structure has an intrinsic affinity to deform into, provided that there are no substantial nonlinear prebuckling effects present. That is, in the absence of substantial nonlinear prebuckling effects, the linear-bifurcation eigenvalues represent when (at what load level) and where (what configurations) strong interactions between compressive membrane stresses and normal displacements are likely to be present that can lead to a sudden, dynamic change in shell deformation pattern. When nonlinear prebuckling effects are significant, substantial normal displacements occur as the loading increases that significantly reduce, or eliminate, the amount of membrane strain energy that is stored in the shell that is available for a dynamic change in deformation state. In addition, the four-mode imperfection was selected because of the statement given by Bushnell[5] that suggests that premature failure of shell structures that exhibit a short-wavelength response can be activated or triggered by imperfections with a similar short-wavelength shape. Thus, the four-mode imperfection is expected to represent adequately a preferred direction of early departure from the primary equilibrium path should the structure have a tendency to do so.

Results are presented in Figs. 10 and 11 that show the nonlinear deformations that were obtained from STAGS analyses of a geometrically perfect shell and a geometrically imperfect shell with an imperfection-amplitude-to-wall-thicknessratio $A/t = 1$, respectively. The thickness t in the ratio A/t is the average wall thickness

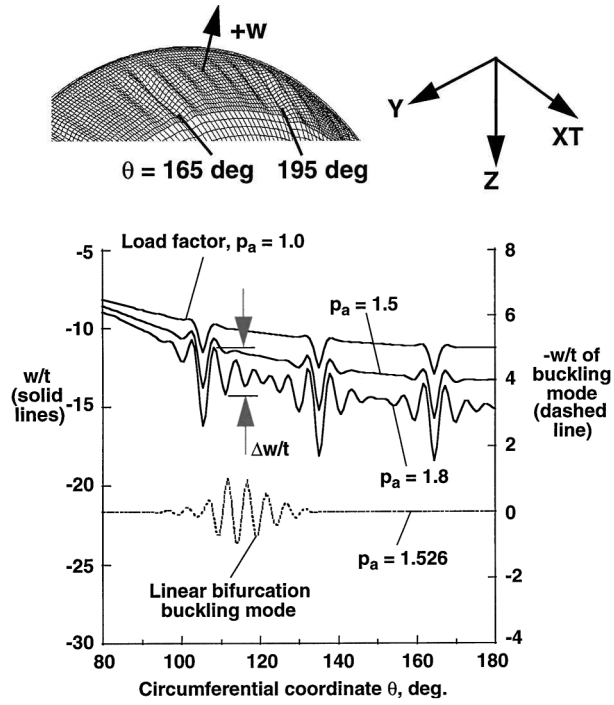

Fig. 10 Nondimensional normal displacement *w/t* of geometrically perfect aft dome; *t* = 0.090 in. and *XT* = 885 in.

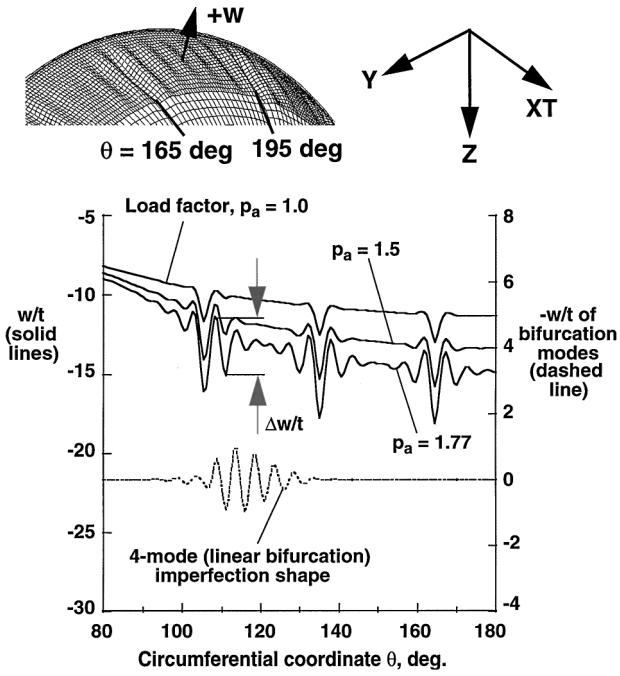

Fig. 11 Nondimensional normal displacement *w/t* of geometrically imperfect aft dome; imperfection-amplitude-to-wall-thickness ratio *A/t* = 1, *t* = 0.090 in., and *XT* = 885 in.

of the top part of the aft dome ($t = 0.090$ in.). The results shown in Fig. 11 were obtained by using the four-mode imperfection that was described earlier in the present paper. For this imperfection, the shape is given by summing the first four eigenvectors, scaling the sum to give $A/t = 1$ and then multiplying by -1. The negative of the linear combination was used as the imperfection shape because it was found to provide a stronger nonlinear interaction with the compressive stresses in the shell wall than the positive-valued linear combination. The results shown in Figs. 10 and 11 are for nonlinear solutions that were obtained by increasing the load factors p_a and p_b simultaneously to a value of one, and then holding p_b constant while increasing the magnitude of the load factor p_a.

The nondimensional normal displacements w/t along the circumference of the aft dome shell wall at $XT = 885$ in. and from $\theta = 80$ to 180 deg are represented by the solid lines in Figs. 10 and 11 for values of the load factor p_a approximately equal to 1.0, 1.5, and 1.8. Moreover, the line given by $\theta = 180$ deg in Figs. 10 and 11 is essentially a line of reflective symmetry for the nonlinear-response curves. Overall, negative values of the normal displacements are indicated by the left-hand ordinate for these three load factors. These results are negative because of the contraction of the aft dome that is caused primarily by the LO_2 thermal load (shrinkage). The linear-bifurcation buckling mode and half of the four-mode imperfection are represented by the dashed lines in Figs. 10 and 11, respectively, with normalized amplitudes given by the right-hand ordinate of the figures. The third linear-bifurcation mode is obtained by reflection of the dashed line in Fig. 10 about the line $\theta = 180$ deg. Similarly, the second half of the four-mode imperfection is obtained by reflection of the dashed line in Fig. 11 about the line $\theta = 180$ deg. The linear-bifurcation buckling mode and the half of the four-mode imperfection shown in Figs. 10 and 11 are very similar and are included in the figures to give an indication of how the imperfection shape influences the nonlinear solution.

The solid lines shown in Figs. 10 and 11 indicate a short-wavelength bending response in the circumferentially compressed part of the aft dome that extends from approximately $\theta = 95$ to 180 deg. Although they are not shown in Figs. 10 an 11, the deformations are symmetric about the right-hand axis and actually extend to approximately $\theta = 265$ deg. The pattern of the nonlinear deformations are substantially different from the linear-bifurcation buckling mode and the four-mode imperfection and encompass a much larger portion of the dome circumference. However, like the linear-bifurcation buckling mode, the ratio of the largest thickness in the area of the deformation pattern shown in Figs. 10 and 11 to the smallest characteristic length of the buckle pattern is less than 0.1, which suggests that finite elements that are based on classical thin-shell theory are adequate. The overall increasing slope trend of the solid lines in Figs. 10 and 11 (seen by neglecting the undulations in the curves) is due to the inward displacement of the shell wall that is caused by the increase in pressure as p_a is increased to values greater than one in the nonlinear analysis. This nonlinear effect is not accounted for in a linear-bifurcation buckling analysis, and, as a result, the dashed lines do not exhibit a similar overall increasing slope trend.

The results presented in Figs. 10 and 11 predict a stable, but highly wrinkled, nonlinear, elastic response at a load level greater than the load level predicted by the linear-bifurcation buckling analysis ($p_a = 1.526$). From a generic point of view, the results indicate that a design based on a linear-bifurcation buckling analysis and buckling-load knockdown factor, assuming that a meaningful one is available, would be overly conservative. At the operational load level given by $p_a = 1$, the results predict significant nonlinear prebuckling deformations at values close to $\theta = 105$, 135, and 165 deg, which are the locations of the meridional weld lands in that part of the aft dome. As the load is increased, substantial bending deformations (indicated by the waviness of the curves) develop and grow in the shell wall between the weld lands, which reduces the apparent circumferential stiffness of the aft dome. The largest bending deformations shown in Figs. 10 and 11 are predicted to occur at the locations of the meridional weld lands and are thought to be slightly overpredicted because the weld lands are represented by discrete stringers (concentrated stiffnesses). Although it is difficult to see in Figs. 10 and 11, these results also indicate that a geometrical imperfection in the shape of the first four linear-bifurcation modes and with a small negative amplitude does amplify the severity of the bending deformations (e.g., compare the magnitudes of $\Delta w/t$ shown in the Figs. 10 and 11) and causes the growth of the bending deformations to start at slightly lower load levels. The von Mises stresses in the aft dome shell walls were calculated for the higher load factors shown in Figs. 10 and 11 and were found to be below the approximately 70,000 psi yield stress of the aluminum–lithium material.

The reduction in the apparent circumferential stiffness of the aft dome is shown more explicitly in Figs. 12 and 13 for the geometrically perfect and imperfect shells, respectively. In Figs. 12 and 13,

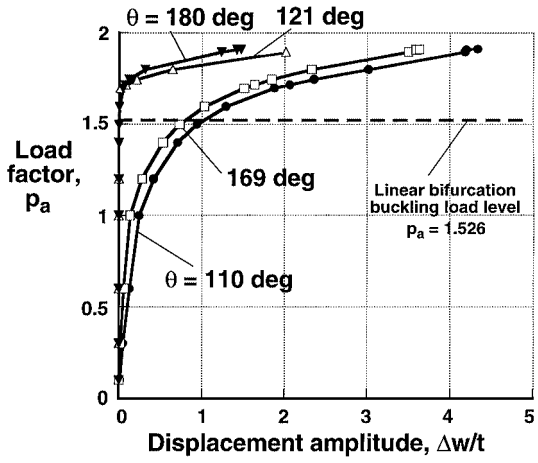

Fig. 12 Local nondimensional normal displacement amplitudes $\Delta w/t$ of geometrically perfect aft dome at XT = 885 in.; t = 0.090 in.

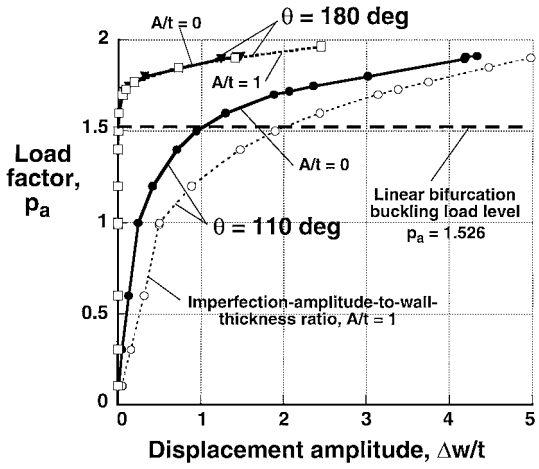

Fig. 13 Local nondimensional normal displacement amplitudes $\Delta w/t$ of geometrically perfect and imperfect aft domes at XT = 885 in.; t = 0.090 in.

the intensities of the bending deformations along $XT = 885$ in. that are shown in Figs. 10 and 11 are given as a function of the load factor p_a for several circumferential locations. The intensity of the bending deformations is given by the nondimensional quantity $\Delta w/t$, which is the normalized amplitude of an undulation in the curves at a specific value of θ. For example, $\Delta w/t$ is shown in Figs. 10 and 11 for approximately $\theta = 110$ deg. Four curves are presented in Fig. 12 for the geometrically perfect shell that correspond to values of $\theta = 110$ (filled circles), 121 (unfilled triangles), 169 (unfilled squares), and 180 deg (filled triangles). The curves for $\theta = 110$ and 169 deg correspond to the severe bending deformations next to two of the weld lands, and the other two curves correspond to locations that are approximately midway between weld lands. Similarly, the curves for $\theta = 110$ and 180 deg that are shown in Fig. 12 are also shown in Fig. 13 (solid curves) along with the corresponding curves for the imperfect shell with $A/t = 1$ (dashed curves). The horizontal dashed lines shown in Figs. 12 and 13 represent the linear-bifurcation buckling-load level ($p_a = 1.526$).

The results shown in Figs. 12 and 13 indicate that the bending deformations near the meridional weld lands dominate the response of the aft dome; that is, $\Delta w/t$ grows at the highest rate at $\theta = 110$ and 169 deg. Moreover, the results predict that this effect is much more pronounced for the imperfect shell with $A/t = 1$. The curves for $\theta = 110$ deg were included in Fig. 13 because they show the greatest effect of the four-mode imperfection. In contrast, the effect of the imperfection is shown to be benign for the point between weld lands at $\theta = 180$ deg. Corresponding results were obtained for $\theta = 121$ and 169 deg. These results show that the effect of the imperfection at $\theta = 121$ deg (between weld lands) was slightly larger than that shown in Fig. 13 for $\theta = 180$ deg but much smaller than that shown for $\theta = 110$ deg (next to a weld land). Also, the results show that the effect of the imperfection at $\theta = 169$ deg (next to a weld land) is benign.

All of the results shown in Figs. 12 and 13 show a monotonically increasing nonlinear response and predict that the shell can support loads greater than the critical buckling load predicted by an elastic, linear-bifurcation buckling analysis. As $\Delta w/t$ increases, the apparent circumferential stiffness decreases, and as a result, the positive-valued constant of proportionality between an increment in load and the corresponding increment in displacement amplitude decreases. This trend is manifested by the reduction in slope of the load vs displacement-amplitude curves. This type of response is similar to the response presented for the prelaunch loading condition with full LO_2 and LH_2 tanks[1,2] and to the response reported by Stevens et al.[6] for cylindrical shells subjected to combined internal pressure and a pure bending moment. The results in Ref. 6 indicate that the amplitude of the short-wavelength deflection grows rapidly as the load increases and approaches a critical value. At the critical value of the load, the load-deflection response curve approaches a horizontal tangent that corresponds to a local collapse mode of the cylinder. Mathematically, the horizontal tangent indicates that unbounded growth of the displacement occurs for an infinitesimal increase in the load. It is expected that the curves shown in Figs. 12 and 13 would approach a horizontal tangent as $\Delta w/t$ increases until a redistribution in load occurs within the aft dome. As a horizontal tangent in a load vs displacement-amplitude curve is approached, the region of the shell containing the bending deformations becomes incapable of supporting additional load, and the compressive load is redistributed to another portion of the aft dome. If other parts of the dome cannot support the redistributed compressive load or if excessive yielding occurs, the shell will collapse.

The results presented in Figs. 10–13 indicate that large local, elastic bending deformations may occur in the shell wall for loads that are much smaller than the local collapse load and may cause the TPS to debond from the shell wall and fail. This mode of failure is of great importance in the design of the TPS for contemporary space vehicles. The results presented in Fig. 14 provide a means of gaining insight into the performance of the TPS and illustrate a method that could be used for future launch vehicles. These results give estimates of the local radius of curvature ρ for the bending deformation in the aft dome at $XT = 885$ in. and $\theta = 109$ deg (next to a weld land). The local radius of curvature ρ was calculated with STAGS as close as possible to the crests of the deformations patterns where the slope $w' = 0$. At this location, the radius of curvature is given by $\rho = |w''|^{-1}$, where w is the normal displacement and the prime marks in the equation denote differentiation with respect to a local Cartesian surface coordinate. The filled circles shown in Fig. 14 correspond to results for the geometrically perfect shell, and the unfilled circles correspond to results for the geometrically imperfect shell with an imperfection-amplitude-to-wall-thickness ratio of $A/t = 1$.

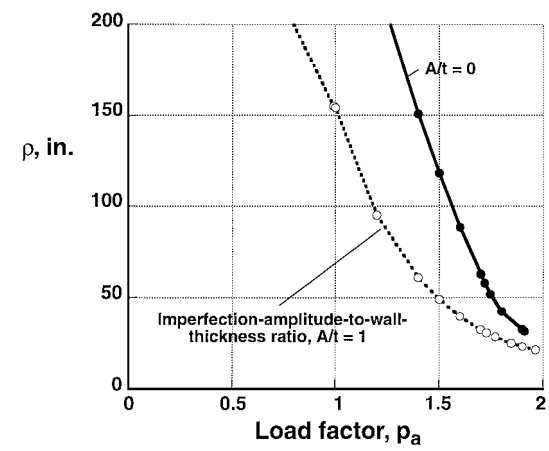

Fig. 14 Local radii of curvature ρ of bending deformation at XT = 885 in. and θ = 109 deg for geometrically perfect and imperfect aft domes; t = 0.090 in.

The results in Fig. 14 demonstrate that the geometric imperfection amplitude has a significant influence on the local radius of curvature of the shell wall. For example, if a given TPS is known to debond from the shell wall at a value of $\rho = 100$ in., the maximum load factor is reduced from a value of approximately 1.6 for the geometrically perfect shell to 1.3 for the geometrically imperfect shell with $A/t = 1$. However, a large-amplitude, short-wavelength imperfection of this type is unlikely to be present in a piece of high-precision flight hardware. Thus, the radius-of-curvature results for the perfect shell are much more practical than the corresponding results for the imperfect shell because such large imperfections would most likely be identified during inspection of the shell.

Despite the concerns about acute imperfection sensitivity that is sometimes associated with the presence of several, nearly equal linear-bifurcation eigenvalues, the results presented in Figs. 10–13 indicate a stable nonlinear response for the imperfect shell, which has a relatively large imperfection amplitude. Moreover, the results indicate the presence of substantial nonlinear prebuckling deformations that diminish the significance of the closely spaced linear-bifurcation eigenvalues. This trend is consistent with the qualitative guidelines for imperfection sensitivity given in Ref. 5 and is likely to be encountered in the design of future liquid-fuel launch vehicles. The trend can be explained by noting that, as the nonlinear prebuckling deformations grow with increasing load, they represent a perturbation of the shell geometry and a local change in the stress state that is not represented physically by the linear-bifurcation eigenvalues. The stability of the wrinklelike deformation state is at least partially attributed to the compression region being a local region that is more likely to cause a benign internal load redistribution in the presence of nonlinear prebuckling deformations than a sudden mode change or collapse. This explanation is also consistent with qualitative guidelines for imperfection sensitivity that are presented in Ref. 5 and was confirmed in the analyses by performing bifurcation analyses from the nonlinear configurations at several of the higher load levels. The behavior of the aft dome of the LO_2 tank is significantly different from that of a compression-loaded cylinder or an externally pressurized sphere that exhibit several nearly equal, or a multiplicity of, linear-bifurcation eigenvalues. A major difference is that the region of compression of the aft dome does not fully envelop the shell, unlike the compression-loaded cylinder or the externally pressurized sphere. This difference facilitates load redistribution in the aft dome without shell collapse or a mode change. For similar, future launch vehicle shell structures that experience compressive stresses over the majority of their areas, an increased imperfection sensitivity caused by modal interaction may be present.

Concluding Remarks

Elastic, linear-bifurcation buckling and nonlinear analyses of the Space Shuttle SLWT LO_2 tank have been presented. The loading details for an important end-of-flight loading condition have been described, and the method used to simulate the loading condition has been discussed. Results have been presented herein that were obtained from complex, large-scale, finite element models of a portion of the Space Shuttle SLWT tank. These results illustrate an important type of nonlinear response for thin-walled shells subjected to combined mechanical and thermal loads that may be encountered in the design of other liquid-fuel launch vehicles. Moreover, the results illustrate the importance of initial shell-wall geometric imperfections on the structural behavior, which is an important consideration in the design of future launch vehicles. One important finding of the present study is that large-scale, high-fidelity finite element models are generally required to predict accurately the linear bifurcation and nonlinear responses, because the corresponding deformation patterns are small compared to the overall size of the structure. Overly coarse, finite element models could miss the response mode entirely.

For the end-of-flight loading condition, linear-bifurcation buckling analyses yielded several nearly equal eigenvalues that correspond to local buckling modes. However, the nonlinear analyses yielded responses that are characterized by a short-wavelength bending deformation that grows in amplitude in a stable manner with increasing load. The overall response of the structure is insensitive to initial shell-wall geometric imperfections, which is, to a large extent, a result of the somewhat localized nature of the compressive stresses in the shell that facilitates stress redistribution instead of collapse of the shell wall. An important consequence of these results that may be applicable to the design of future liquid-fuel launch vehicles is that a design based on the traditional approach of computing a linear-bifurcation buckling load and accounting for imperfection sensitivity with a buckling-load knockdown factor is likely to be overly conservative. This conclusion is especially true when buckling-load knockdown factors are not well known and must be contrived in some manner.

The local bending deformations that were obtained from the nonlinear analyses, which are significantly different from the linear-bifurcation modes, appear in the aft elliptical dome of the LO_2 tank and do not lead to a general instability mode, but may cause failure of the TPS. Because this concern, results have been presented herein that can be used to estimate the load level at which a TPS failure is likely to occur. The method that was used to assess the TPS requires a nonlinear analysis to predict accurately the shell wall deformations and constitutes a method that can be used to assess the performance of TPS systems for future launch vehicles. Imperfection sensitivity analyses have also been presented that indicate that the aft dome does not exhibit a nonlinear collapse mode associated with the interaction of nearly equal linear-bifurcation modes for load levels below approximately 1.9 times the operational load level. However, the results do predict that the severity of some of the local deformations may be significantly affected by a localized initial geometric imperfection.

Acknowledgments

The authors would like to express their thanks to V. O. Britt, Walter L. Heard Jr. (retired), Charles C. Rankin, Michael Quiggle, and Neil Otte of Gulf Stream Aerospace, Inc., NASA Langley Research Center, Lockheed Martin Missiles and Space Company, Lockheed Martin Michoud Space Systems Division, and the NASA Marshall Space Flight Center, respectively, for their technical support.

References

[1] Nemeth, M. P., Britt, V. O., Collins, T. J., and Starnes, J. H., Jr., "Nonlinear Analysis of the Space Shuttle Superlightweight External Fuel Tank," NASA TP-3616, Dec. 1996.

[2] Nemeth, M. P., Britt, V. O., Young, R. D., Collins, T. J., and Starnes, J. H., Jr., "Nonlinear Behavior of Space Shuttle Superlightweight Liquid-Oxygen Tank Under Prelaunch Loads," *Journal of Spacecraft and Rockets*, Vol. 36, No. 6, 1999, pp. 788–803.

[3] Brogan, F. A., Rankin, C. C., and Cabiness, H. D., "STAGS User Manual," Lockheed Martin Missile and Space Co., Rept. LMSC P032594, Palo Alto, CA, 1994.

[4] Young, R. D., and Rankin, C. C., "Modeling and Nonlinear Structural Analysis of a Large-Scale Launch Vehicle," *Journal of Spacecraft and Rockets*, Vol. 36, No. 6, 1999, pp. 804–811.

[5] Bushnell, D., "Static Collapse: A Survey of Methods and Modes of Behavior," *Collapse Analysis of Structures*, PVP-Vol. 84, American Society of Mechanical Engineers, Fairfield, NJ, 1984, pp. 30–32.

[6] Stephens, W. B., Starnes, J. H., Jr., and Almroth, B. O., "Collapse of Long Cylindrical Shells Under Combined Bending and Pressure Loads," *AIAA Journal*, Vol. 13, No. 1, 1975, pp. 20–25.

H. L. McManus
Associate Editor